Article

Bifunctional Co_3O_4/g-C_3N_4 Hetrostructures for Photoelectrochemical Water Splitting

Syeda Ammara Shabbir,* Iqra Ali, Muhammad Haris, Hamid Latif, Aneeqa Sabah, Ali S. Alshomrany, and Youssef Bakkour

Cite This: ACS Omega 2024, 9, 21450−21458

Read Online

ACCESS | Metrics & More | Article Recommendations

ABSTRACT: This study explored the synergistic potential of photoelectrochemical water splitting through bifunctional Co_3O_4/g-C_3N_4 heterostructures. This novel approach merged solar panel technology with electrochemical cell technology, obviating the need for external voltage from batteries. Scanning electron microscopy and X-ray diffraction were utilized to confirm the surface morphology and crystal structure of fabricated nanocomposites; Co_3O_4, Co_3O_4/g-C_3N_4, and Co_3O_4/Cg-C_3N_4. The incorporation of carbon into g-C_3N_4 resulted in improved catalytic activity and charge transport properties during the visible light-driven hydrogen evolution reaction and oxygen evolution reaction. Optical properties were examined using UV−visible spectroscopy, revealing a maximum absorption edge at 650 nm corresponding to a band gap of 1.31 eV for Co_3O_4/Cg-C_3N_4 resulting in enhanced light absorption. Among the three fabricated electrodes, Co_3O_4/Cg-C_3N_4 exhibited a significantly lower overpotential of 30 mV and a minimum Tafel slope of 112 mV/dec This enhanced photoelectrochemical efficiency was found due to the established Z scheme heterojunction between Co_3O_4 and gC_3N_4. This heterojunction reduced the recombination of photogenerated electron−hole pairs and thus promoted charge separation by extending visible light absorption range chronoamperometric measurements confirmed the steady current flow over time under constant potential from the solar cell, and thus it provided the effective utilization of bifunctional Co_3O_4/g-C_3N_4 heterostructures for efficient solar-driven water splitting.
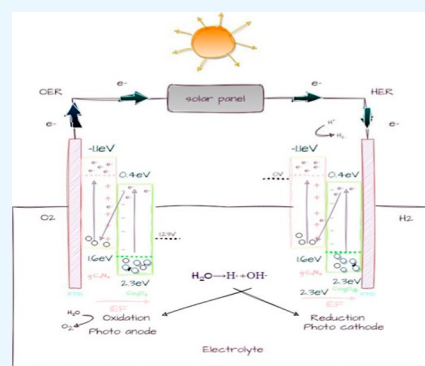
1. INTRODUCTION

The quest for sustainable and clean energy sources is of paramount importance in the face of growing global energy demands and ever-increasing environmental concerns.[1,2] Among the various energy conversion technologies, hydrogen production via water splitting has emerged as a promising pathway toward a cleaner and more sustainable future.[3,4] Hydrogen, as a clean and efficient energy carrier, has the potential to revolutionize our energy landscape.[5] Tandem photoelectrochemical water splitting is a rapidly evolving field that offers significant promise in the pursuit of efficient and environmentally friendly hydrogen production.[6,7] One of the central challenges in the field of photoelectrochemical water splitting is the need for efficient materials that can drive the reactions with high performance under solar illumination.[8,9] Conventional photoactive materials, such as single semiconductor materials, often exhibit limitations in terms of charge separation, light absorption, and catalytic activity.[10,11] Achieving a delicate balance between these properties in a single material remains a substantial challenge.[12] Additionally, the instability of some materials under harsh operating conditions can hinder their long-term application.[13] Thus, the development of new materials and architectures that can

overcome these challenges is essential for advancing the field.[14,15]

The materials used in the context of photoelectrochemical water splitting have included various semiconductors, such as TiO_2, WO_3, and $BiVO_4$, among others.[16,17] While these materials have demonstrated photocatalytic activity, they often suffer from significant drawbacks.[18] For instance, TiO_2 exhibits excellent stability but has limited absorption in the visible spectrum, thereby underutilizing solar energy.[19] WO_3, while responsive to visible light, is prone to photocorrosion in aqueous environments.[20] $BiVO_4$, another promising material, possesses a suitable band gap but suffers from limited charge separation efficiency.[21] Furthermore, the materials commonly employed for water splitting often face challenges in effectively promoting both the water oxidation and reduction reactions concurrently.[9,22] The band alignment between materials for
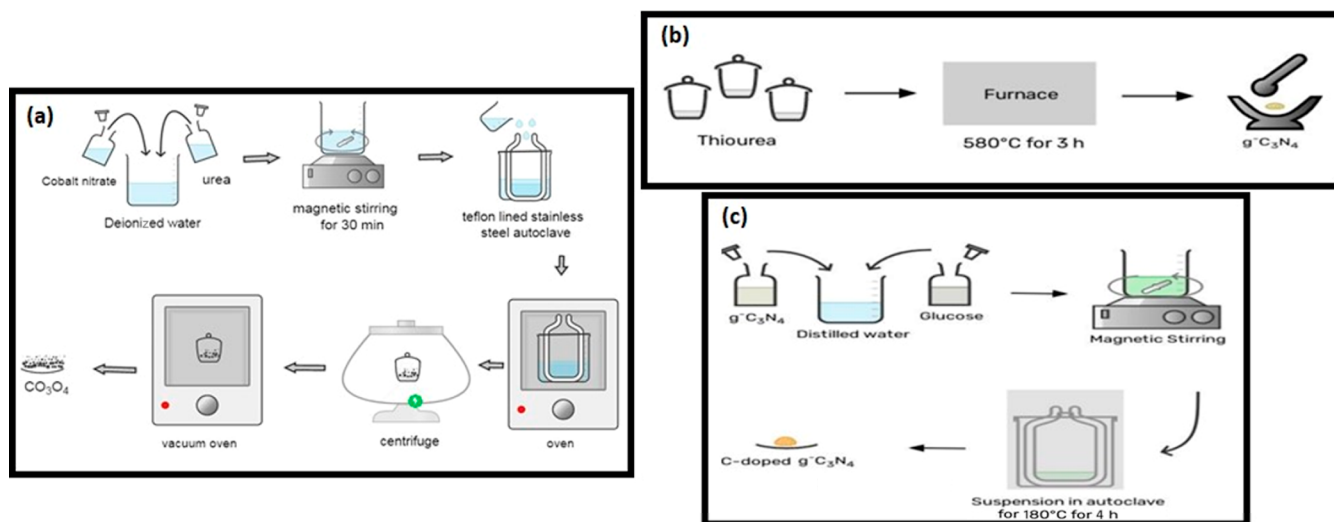
Figure 1. Schematics for synthesis of CO_3O_4, gC_3N_4, and C-doped gC_3N_4.

each half-reaction is crucial but hard to optimize in conventional single-material systems.[23] This has led to the exploration of heterostructures, where different materials with complementary properties can be combined to address these shortcomings.[24,25]

In response to the limitations of previous materials, bifunctional $Co_3O_4/G-C_3N_4$ heterostructures have emerged as an exciting avenue for advancing tandem photoelectrochemical water splitting.[26,27] Co_3O_4, a transition-metal oxide, is known for its high electrical conductivity and chemical stability, making it a suitable candidate for catalyzing the water oxidation reaction.[28,29] $G-C_3N_4$, on the other hand, is a metal-free and eco-friendly semiconductor with excellent light absorption properties and efficient electron−hole separation.[30,31] The combination of these materials in heterostructures facilitates efficient charge separation and transfer, minimizing electron−hole recombination and optimizing overall photocatalytic performance.[32,33]

It is worth noting that in this work, the conventional use of a battery to store energy has been replaced by the utilization of the potential generated by solar cells.[34] This introduces a more economical and reliable method for hydrogen production, aligning with the principles of sustainability and clean energy. Furthermore, the bifunctional property of $Co_3O_4/G-C_3N_4$ heterostructures plays a pivotal role.[35] These materials are fabricated using a drop-casting technique, providing a cost-effective and scalable means of production.[36] By using these heterostructures as both the photoanode and photocathode, instead of relying on costly platinum-based cathodes, the research contributes to a more sustainable and economically viable solution for tandem water splitting.[37] The bifunctional nature of these materials enables the efficient utilization of solar energy and enhances the overall photocatalytic activity.[38]

This study not only provides an innovative solution to solar-driven water splitting but also introduces a novel approach to design advanced bifunctional photoelectrodes CgC_3N_4/Co_3O_4 for both the oxygen evolution reaction (OER) and hydrogen evolution reaction (HER), demonstrating the potential for harnessing renewable energy sources without the need for energy storage via batteries. The $Co_3O_4/g-C_3N_4$ z scheme-based heterostructures, along with their bifunctional properties, opens new avenues for enhancing the efficiency and

sustainability of hydrogen production, thereby contributing to the broader goals of clean energy and environmental preservation.[39,40] Herein, a facile fabrication method was proposed to obtain heterojunction by altering sequential layering of Co_3O_4 and $g-C_3N_4$ for photoanodes and photocathodes. Co_3O_4 offers high electrical conductivity and chemical stability, making it ideal for catalyzing the water oxidation reaction and $g-C_3N_4$ doped with carbon demonstrates enhanced photocatalytic activity for catalyzing the water reduction reaction.[41−43] Overall, the composite offered efficient light absorption and electron−hole separation to avoid recombination during the OER and HER and thus is utilized as a highly active catalytic material in photoelectrochemical systems. The utilization of carbon doped g-C_3N_4 provided a unique approach to improve the performance of photoanodes in the quest for more sustainable hydrogen production.

2. METHODOLOGY

For Co_3O_4 nanoparticle fabrication, cobalt nitride $[Co(NO_3)_2 \cdot H_2O]$ with a mass of 0.6 g and urea (0.6 g) were combined in a solution as shown in schematics in Figure 1a. This solution, composed of 100 mL of deionized water, was mixed at room temperature for a duration of 30 min. The resultant mixture was then moved to a 60 mL stainless-steel autoclave lined with Teflon. The method employed here is commonly termed the hydrothermal synthesis method. During this process, the temperature at which the synthesis occurred was 180 °C. This temperature was sustained for a period of 72 h. Subsequent to the reaction time, the solid precipitate formed was isolated through centrifugation. To eliminate any lingering residual ions, a thorough cleansing process was carried out using distilled water and ethanol. The final solid product was then subjected to vacuum drying at 60 °C overnight. The graphitic carbon nitride ($g-C_3N_4$) was produced using a thermal polymerization method with thiourea, as shown in Figure 1b. To begin the process, 7.6 g of thiourea was carefully placed inside a porcelain crucible, which was then securely sealed using aluminum foil. Subsequently, the crucible was heated in a muffle furnace, maintaining a temperature of 580 °C for a duration of 3 h. The temperature was gradually raised at a rate of 3.5 °C per minute. After the completion of the heating
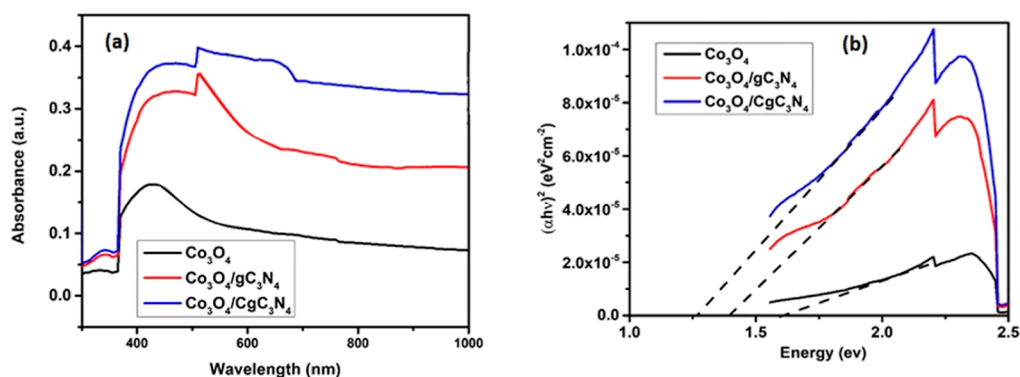
Figure 2. (a) UV−visible spectroscopic analysis and (b) Tauc plots of Co_3O_4, $Co_3O_4/g\text{-}C_3N_4$, and $Co_3O_4/Cg\text{-}C_3N_4$.

process, the crucible was allowed to cool, and the resulting product of $g\text{-}C_3N_4$ was finely powdered using a porcelain mortar and subsequently collected for further use. The method employed in the preparation of carbon-doped $g\text{-}C_3N_4$ composites is known as hydrothermal synthesis, as shown in Figure 1c. This method involves reacting 0.4 g of $g\text{-}C_3N_4$ and 0.0025 g of glucose in 20 mL of distilled water, stirring for 2 h, then subjecting the mixture to 180 °C in an autoclave for 4 h. After hydrothermal treatment, the resulting suspension is dried at 90 °C for 12 h, yielding the carbon-doped $g\text{-}C_3N_4$ (Cg-C_3N_4). Hydrothermal synthesis facilitates the integration of glucose into the $g\text{-}C_3N_4$ structure, enhancing the material properties through controlled crystalline growth and morphology. These fabricated materials Co_3O_4, gC_3N_4, and C-gC_3N_4 were dissolved in dimethyl sulfoxide (DMSO) and were drop cast on fluorine-doped tin oxide (FTO) substrates for fabrication of photoanodes and photocathodes. Three *z* scheme heterostructure-based photoanodes were fabricated Co_3O_4, Co_3O_4/gC_3N_4, and $Co_3O_4/C\text{-}gC_3N_4$ by sequential layering with Co_3O_4 as a top layer. Similarly, three photocathodes were fabricated; gC_3N_4, gC_3N_4/Co_3O_4, and C-gC_3N_4/Co_3O_4 by sequential layering with gC_3N_4 as a top layer for photocathodes.

3. CHARACTERIZATION TECHNIQUES

Surface morphology and structural features of the fabricated catalytic materials Co_3O_4, gC_3N_4, and C-gC_3N_4 were confirmed through scanning electron microscopy (SEM) and X-ray diffraction (XRD) analysis. Optical characteristics, particularly the determination of the band gap, were assessed using UV−visible spectroscopy. Subsequently, electrochemical performance for the HER and OER was evaluated via linear sweep voltammetry (LSV) using Versa STAT 3F Potentiostat, Ametek. The platinum was used as the counter electrode and saturated calomel electrode(SCE) was used as a reference electrode. LSV was then plotted versus NHE using $E_{NHE} = E_{SCE} + 0.059 \, pH + 0.241$. LSV were obtained with a 25 mV s^{-1} scan rate. Furthermore, chronoamperometry was conducted to showcase the improved performance of the $Co_3O_4/G\text{-}C_3N_4$ heterostructure using a solar cell in tandem photoelectrochemical water splitting, underlining its prospective for practical applications. Chronoamperometric analysis was utilized to monitor steady current flow under constant potential conditions, highlighting the enhanced performance of the $Co_3O_4/CG\text{-}C_3N_4$ heterostructure in tandem photoelectrochemical water splitting. The photoelectrochemical (PEC) measurements involved employing an electrochemical work-

station in a 1 M potassium hydroxide (KOH) electrolyte solution at a neutral pH of 7. These assessments were conducted under solar illumination with a solar simulator (Newport Oriel Solar 3A class AAA, 64023 A) under AM 1.5 G illumination (1000 W/m^2).

4. RESULTS AND DISCUSSION

UV−visible spectroscopy analysis was conducted to investigate the optoelectronic properties of cobalt oxide (Co_3O_4)-based nanocomposites. Figure 2a illustrates the absorption spectra of the three fabricated nanocomposites; Co_3O_4, Co_3O_4-$g\text{-}C_3N_4$, and $Co_3O_4/Cg\text{-}C_3N_4$. A wider range of UV and visible light is being absorbed by fabricated samples, indicating their capability to interact with and absorb light. Maximum wavelength (λ_{max}) corresponds to the wavelength at which a substance exhibits its most pronounced photon absorption, representing the peak point on the *y*-axis of the absorption spectrum. Specifically, the λ_{max} value for Co_3O_4 is measured to be 450 nm, while its absorption edge extends to 520 nm within the visible spectrum range. In contrast, the $Co_3O_4/g\text{-}C_3N_4$ composite demonstrated a λ_{max} value of 510 nm, accompanied by a notably enhanced absorption edge at 620 nm, falling within the wavelength range of 200 to 800 nm. This significant improvement can be attributed to the incorporation of $g\text{-}C_3N_4$ into the composite structure. The introduction of $g\text{-}C_3N_4$ leads to a substantial increase in absorption intensity compared to the individual Co_3O_4 component. Furthermore, the $Co_3O_4/C\text{-}g\text{-}C_3N_4$ composite catalyst showcased the most heightened absorption intensity in the UV−visible light range, and its absorption edge is expanded to 650 nm. This augmentation allowed for the absorption of a wider range of photon wavelengths. Consequently, the λ_{max} value for this composite is measured at 500 nm, signifying its capacity to effectively absorb light across this spectrum. Table 1 demonstrates the absorption edge values for the Co_3O_4-based nanocomposites.

Enhancing the photocatalytic efficiency involves creating a heterojunction between Co_3O_4 and $g\text{-}C_3N_4$, along with integrating Cg-C_3N_4 into the composite catalyst. This integration leads to a higher density of energy states, effectively

Table 1. Absorption Edge and Band Gap Values for the Co_3O_4-Based Heterostructures

electrodes	absorbance edge (nm)	band gap (E_g)
Co_3O_4	520 nm	1.61 eV
$Co_3O_4/g\text{-}C_3N_4$	620 nm	1.43 eV
$Co_3O_4/C\text{-}g C_3N_4$	650 nm	1.31 eV
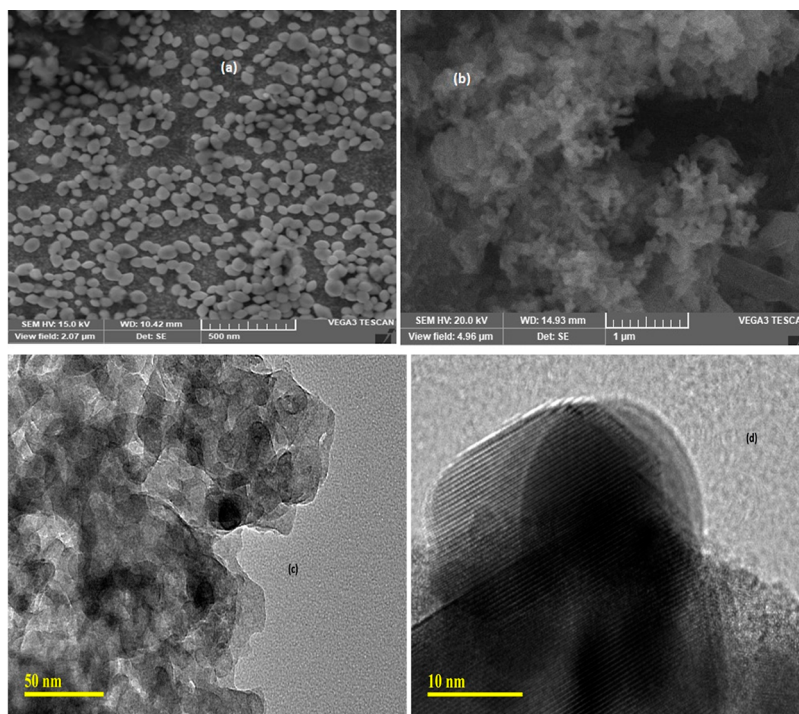
Figure 3. (a,b) SEM images of composite Co_3O_4 and Co_3O_4/g-C_3N_4 and (c,d) TEM image of Co_3O_4/g-C_3N_4 composite.

curbing the recombination rate of pristine Co_3O_4 and thereby reducing its energy band gap. This modification also caused a favorable shift in the optical absorption spectrum toward longer wavelengths, thus promoting electron transitions. Consequently, the composite catalyst exhibited improved potential for visible-light-driven photocatalysis due to its enhanced optical absorption characteristics. Moreover, the fabricated heterostructure-based electrodes generated an increased quantity of electron−hole pairs, achieving improved charge carrier separation. This, in turn, resulted in a notable decline in the recombination rate of electron−hole pairs, contributing to a heightened photocatalytic efficiency. Exploring the optical band gap holds significant importance in evaluating the viability of photocatalytic electrodes. The determination of absorbance spectra and the values of band gap energy were carried out using the Tauc relation, specifically analyzing the relationship between $(ahv)^2$ and hv, as shown in Figure 2b.

In Figure 2b, the band gap of the Co_3O_4 electrode is observed to be 1.61 eV. Meanwhile, for Co_3O_4/g-C_3N_4 and Co_3O_4/Cg-C_3N_4 composites, the band gaps are measured to be 1.43 and 1.31 eV, respectively. Table 1 demonstrates the energy band gap values for all of the fabricated electrodes. This decrease in the band gap from 1.61 to 1.31 eV implies a significant enhancement in optical absorption, resulting in a broader absorption spectrum. This expansion in the absorption spectrum enhanced the production of electron−hole pairs, thereby contributing to the enhancement of photocatalytic efficiency.

Spherical nanoparticles like structure of Co_3O_4 uniformly distributed throughout is shown in Figure 3a. It revealed well-distributed Co_3O_4 nanoparticles within a size range of about 50 nm. Figure 3b confirms the sheet-like surface morphology of g-C_3N_4 and particle-like structure confirming the surface morphology of Co_3O_4. These Co_3O_4 particles effectively enveloped g-C_3N_4, establishing a direct and close interaction

with its surface. The presence of g-C_3N_4 multilayers within the composite indicates the thorough integration of both substances, leading to the formation of a distinctive heterostructure, which reduced the electron hole recombination rate and hence enhanced the utility of visible light-driven photocatalytic activity. Figure 3 c and d represents the TEM image of Co_3O_4/g-C_3N_4 composite and confirmed the spherical shape of Co_3O_4 nanoparticles and sheet-like structure of gC_3N_4.

The crystal structures of the prepared nanocomposites, namely, Co_3O_4, Co_3O_4/g-C_3N_4, and Co_3O_4/C-g-C_3N_4, were analyzed using XRD, as shown in Figure 4. The XRD pattern of the CO_3O_4/g-C_3N_4 heterostructures displayed several distinct diffraction peaks attributed to the presence of crystalline phases within the sample. The positions and intensities of these peaks were utilized to ascertain the crystal structures analysis.
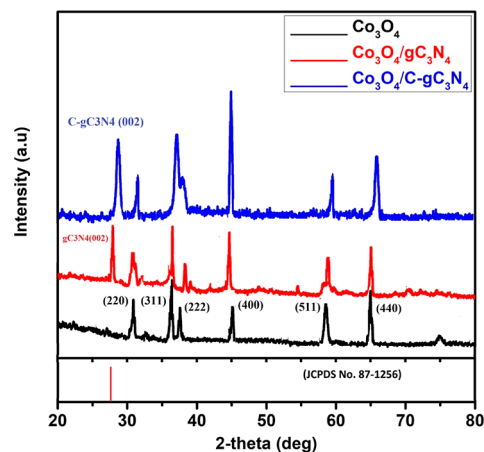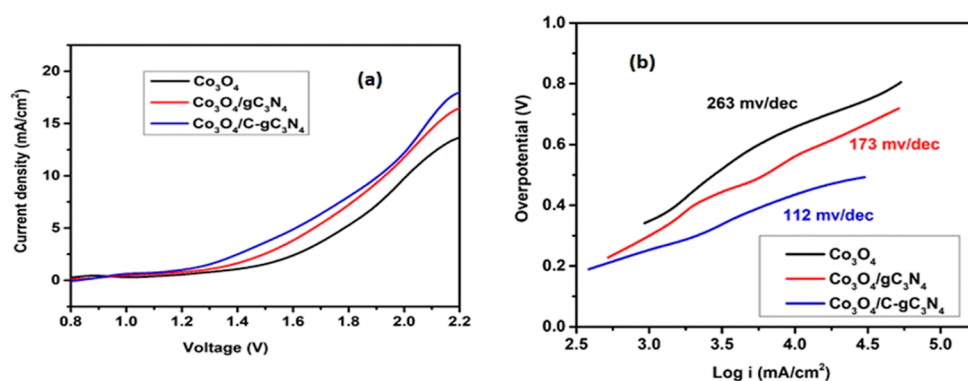

Figure 4. XRD analysis.

Figure 5. (a) LSV analysis and (b) Tafel slopes for the OER.

The XRD patterns of the Co_3O_4 nanocomposite exhibited distinct diffraction peaks corresponding to all of the constituent materials. Particularly, the well-defined diffraction peaks of Co_3O_4 were noticeable at angles of 32°, 36°, 45°, 58°, and 65°, with diffraction planes of (220), (311), (222), (409), (511), and (440), respectively, indicating a strong level of crystallinity. In Co_3O_4/g-C_3N_4 heterostructures, there is a new peak observed in the range of 20°−35°, specifically at angle (002), confirming the presence of g-C_3N_4. Similarly, the Co_3O_4/C-g-C_3N_4 nanocomposite exhibited distinct sharp diffraction peaks of Co_3O_4 and a slight shift in the initial peak (002) of C-g-C_3N_4 was observed, confirming the occurrence of the carbon doping in gC_3N_4 due to a crystal lattice distortion.

To analyze the electrocatalytic characteristics related to a photocurrent density response, the fabricated nanocomposites were utilized as photoanodes and photocathodes in the process of PEC water splitting involving the HER and OER and were subjected to linear sweep voltammetry (LSV). This experimentation took place within a 1 M KOH electrolyte solution while being exposed to 100 mW/cm² illumination. The scan rates utilized were configured at 10 mV/s. Figure 5a shows the LSV analysis for the Co_3O_4, Co_3O_4/g-C_3N_4, and Co_3O_4/C-g-C_3N_4 photoanodes. The Co_3O_4 photoanode showed a limited catalytic efficiency, with a starting potential of 1.45 V and a higher overpotential of 200 mV for the OER. However, an improvement was observed when using Co_3O_4/gC_3N_4. This combination exhibited enhanced activity, displaying a starting onset potential of 1.35 V and a reduced overpotential of 120 mV. Furthermore, the Co_3O_4/C-gC_3N_4 composite demonstrated a significant improvement in onset potential at 1.26 V, along with a notably decreased overpotential of 30 mV. This indicates that less voltage is required for the carbon-doped composite to facilitate charge transfer, making it the most efficient electrode as a photoanode. Tafel slope analysis is shown in Figure 5 b. The corresponding Tafel slopes for the OER are 263 mV/dec for Co_3O_4, 173 mV/dec for Co_3O_4/g-C_3N_4, and 112 mV/dec for Co_3O_4/Cg-C_3N_4 further indicates the efficiency of the electrodes, with lower slopes suggesting a lower overpotential (resistance) and better charge-transfer rate (conductivity), which are crucial for achieving high current density.

Table 2 demonstrates the onset potential, overpotential, and Tafel slopes for Co_3O_4, Co_3O_4/g-C_3N_4, and Co_3O_4/C-g-C_3N_4 photoanodes.

An exploration into the HER involved the execution of a linear sweep voltammetry trial within a 1 M KOH electrolyte

Table 2. Photoelectrochemical Response of LSV for OER

electrodes	onset potential (V)	overpotential (mV)	Tafel slope (mV/dec)
Co_3O_4	1.45	220	263
Co_3O_4/g-C_3N_4	1.35	120	173
Co_3O_4/C-gC_3N_4	1.26	30	112

solution. This experiment took place under the influence of 100 mW/cm² illumination, employing a gradual scanning rate of 10 mV/s.

The LSV results in Figure 6 a show that gC_3N_4 had an onset potential of 0.33 V and a high overpotential of 330 mV. On the other hand, combining Co_3O_4 with g-C_3N_4 resulted in a significant improvement. gC_3N_4/Co_3O_4 achieved an onset potential of 0.23 V, reducing the overpotential to 230 mV compared to the pristine gC_3N_4 semiconductor-based photocathode. Notably, introducing carbon-doped g-C_3N_4 into the photocathode structure (C-gC_3N_4/Co_3O_4) yielded the most efficient outcomes. This configuration exhibited a notable decrease in overpotential to 160 mV, coupled with an onset potential of 0.16 V. The Tafel slopes related to the HER, as illustrated in Figure 6b, exhibit a progressive reduction in overpotential values. This improvement contributes to the increased efficiency of the photocathodes with Tafel slopes of 283, 198, and 121 mV/dec for gC_3N_4, g-C_3N_4/Co_3O_4, and C-g-C_3N_4/Co_3O_4 photocathodes, respectively. Table 3 demonstrates the onset potential, overpotential, and Tafel slope values for gC_3N_4, g-C_3N_4/Co_3O_4, and C-g-C_3N_4/Co_3O_4 photocathodes, respectively.

The transfer and separation of photogenerated charge carriers was analyzed through electrochemical impedance spectrum (EIS), as shown in Figure 7. Figure 7 demonstrates the EIS Nyquist plots for all of the fabricated electrodes: Co_3O_4, gC_3N_4/Co_3O_4, and C-gC_3N_4/Co_3O. The decrease in the radius of the Nyquist plot has been observed with heterojunction formation of gC_3N_4/Co_3O_4. The decrease in the arc radius represents fast reaction kinetics as the internal resistances decreases in the charge-transfer process. With addition of carbon doping of gC_3N_4, the internal resistance becomes weaker, suggesting that the nanocomposite CgC_3N_4/Co_3O_4 exhibited superior charge-transfer ability as the arc radius was smaller than those of other combinations.

For tandem cell measurements, as shown in Figure 8, Co_3O_4, gC_3N_4/Co_3O_4, and C-gC_3N_4/Co_3O_4 were utilized as the photoanode and gC_3N_4, Co_3O_4/gC_3N_4, and Co_3O_4/C-gC_3N_4 were used as the photocathode, respectively, and a solar cell was connected to apply the potential difference. In this context,
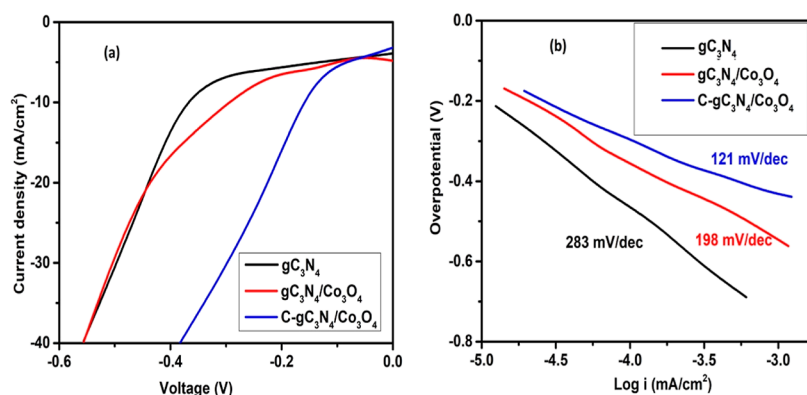
Figure 6. (a) LSV analysis and (b) Tafel slopes for HER.

Table 3. Photoelectrochemical Response of LSV for HER

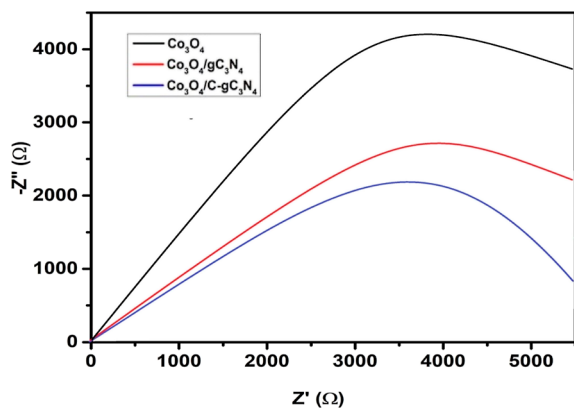| photocathode	onset potential (V)	overpotential (mV)	Tafel slope (mV/dec)
gC_3N_4	0.33	330	283
$g\text{-}C_3N_4/Co_3O_4$	0.23	230	198
$C\text{-}gC_3N_4/Co_3O_4$	0.16	160	121

Figure 7. Electrochemical impedance analysis for Co_3O_4, gC_3N_4/Co_3O_4, and $C\text{-}gC_3N_4/Co_3O_4$ electrodes.
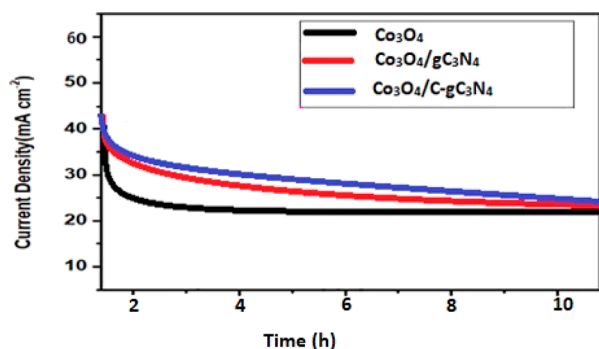

Figure 8. Chronoamperometric curves using a solar cell as the voltage source.

the chronoamperometry technique was employed to monitor the constant potential of 1.23 V applied by the solar panel, which leads to a steady current flow in the system. As time progresses, electron−hole pairs are generated, facilitating oxidation and reduction reactions in the electrochemical cell.

Upon analysis of the graph, it is evident that Co_3O_4 exhibits the lowest current 25 mA/cm², while the heterostructure of

$Co_3O_4/g\text{-}C_3N_4$ displays a higher current of 30 mA/cm² than the pristine Co_3O_4. The composite material, $Co_3O_4/g\text{-}C_3N_4$, demonstrates the maximum current of 35 mA/cm² among the three configurations, showcasing the effectiveness of this merged technology. Table 4 demonstrates the comparison of

Table 4. Chronoamperometric Photoelectrochemical Response of Current

sample name	current density (mA cm²)
CO_3O_4	25
$CO_3O_4/g\text{-}C_3N_4$	30
$CO_3O_4/Cg\text{-}C_3N_4$	35

the current density for the electrodes. In summary, the combination of solar panels and chemical cells in a tandem arrangement enabled the generation of a continuous electrical current for oxidation and reduction reactions in the electrochemical cell. The chronoamperometry technique effectively monitored the constant potential applied by the solar panel, resulting in the observed current flow and enhanced performance of composite $Co_3O_4/Cg\text{-}C_3N_4$ over Co_3O_4 and $Co_3O_4/g\text{-}C_3N_4$ structures.

The charge-transfer mechanism in $C\text{-}gC_3N_4/Co_3O_4$ was proposed based on conduction band (CB) and valence band (VB) potential levels of $C\text{-}gC_3N_4$ and Co_3O_4 using eqs 1 and 2

$$E_{VB} = \chi - E_e + 0.5E_g \tag{1}$$

$$E_{CB} = E_{VB} - E_g \tag{2}$$

where χ, E_e, E_{CB}, E_{VB}, and E_g represents the absolute Mulliken's electronegativity, free electron energy in hydrogen scale (4.50 eV) calculated CB edge, VB position, and energy of band gap, respectively.

Mott−Schottky curves and flat band potentials are shown in Figure 9 for Co_3O_4 and gC_3N_4 From Mott−Schottky plots (Figure 9), it is evident that Co_3O_4 is p-type and gC_3N_4 is n-type. The Mott−Schottky method is a way to determine the flat band position of semiconductors, approximately equal to the CB minimum for the n-type semiconductor and the VB maximum for the p-type semiconductor. In general, the flat band positions are 0.1−0.3 eV lower than the VB edge (VBE) and higher than the CB edge (CBE) of the n-semiconductor.[44] The calculated CB minima and VB maxima from eqs 1 and 2 are close to the flat band position values, as shown in Figure 9. Based on these values, a possible mechanism describing the charge-transfer and separation processes is shown in Figure 10.
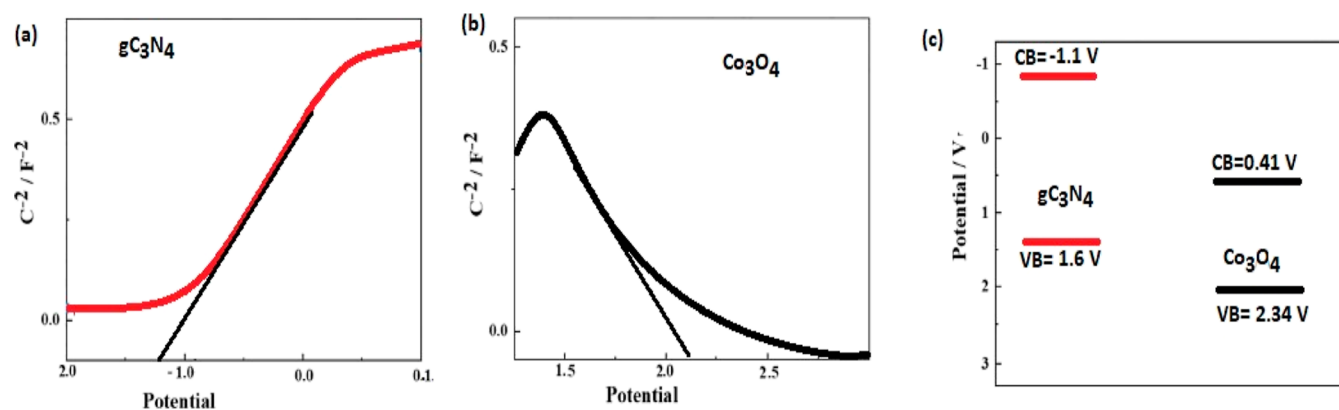
Figure 9. Mott−Schottky curves and band edge positions for gC_3N_4 and Co_3O_4.
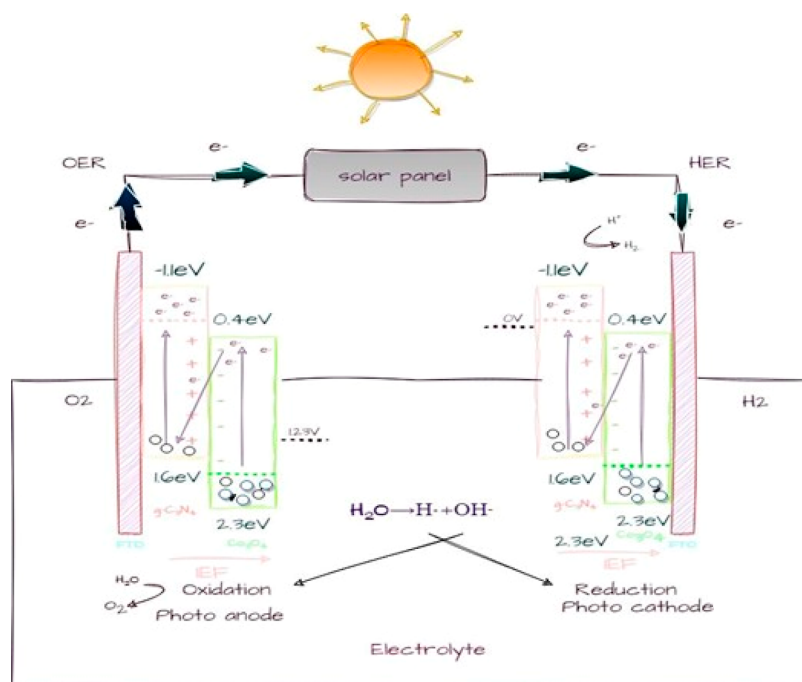

Figure 10. Schematic of photoelectrochemical water splitting technology.

4.1. Working Mechanism of PN Hetrojuctions.

Photoelectrocatalytic performance of water splitting system is determined by the absorption of sunlight and efficient photogenerated charge transfer.[45−47] The possible mechanism of enhanced PEC water splitting for $C-gC_3N_4/Co_3O_4$ and $Co_3O_4/C-gC_3N_4$ as photoanodes and photocathodes, respectively, is illustrated in Figure 10. When P-type (Co_3O_4) and N-type (gC_3N_4) semiconductors were brought together without incident light, their Fermi levels align and form a z scheme heterojunction as shown in figure. Electrons from the N-type semiconductor migrate toward the holes in the P-type semiconductor, creating a depletion region and an internal electric field pointing from N-type to P-type. When light is incident on this P−N heterostructure, electrons are excited and move upward. To prevent recombination, these electrons move in a direction opposite to the electric field, from P to N. Electrons accumulate in the CB of the N-type material, represented by graphitic carbon nitride, while holes accumulate in the VB of the P-type material, represented by cobalt oxide. These holes participate in the oxidation process, while the electrons contribute to the reduction process.

When these heterostructures serve as the photoanode and an external voltage is applied by a solar cell, water molecules break into OH- and H+ ions. The anode, with a positive potential, attracts negative OH-ions, initiating the oxidation process. Four electrons move into the holes of the VB of the cobalt oxide as part of this oxidation. It is crucial that the oxidation potential of OH-ions matches or exceeds the VB of the anode because electrons must transition to a lower energy level during oxidation. The positive side of the solar panel helps capture these electrons lost during oxidation, guiding them through FTO. The same semiconductor is employed as a photocathode, where the reduction potential of H+ ions should be lower than that of the CB of the photocathode. The negative side of the solar panel repels these electrons toward the electrolyte, where H+ ions capture these electrons to produce hydrogen. In this working mechanism, the P−N z scheme heterojunction facilitated efficient charge separation and migration, enabling the oxidation and reduction processes essential for unbiased solar water splitting.

The $Co_3O_4/Cg-C_3N_4$ tandem cell for solar water splitting operated on the principle of harnessing solar energy to

facilitate the splitting of water into hydrogen and oxygen. This process relied on the electron energy diagram and took place in several key steps: the process begins when the Co_3O_4/Cg-C_3N_4 tandem cell absorbs photons from incident sunlight. These photons carry energy that exceeds the band gap of the semiconductors, thereby exciting electrons from the VB to the CB in both Co_3O_4 and Cg-C_3N_4. As a result, electron−hole pairs (excitons) are generated. In the heterojunction formed between Co_3O_4 and Cg-C_3N_4, the electron from the CB of Cg-C_3N_4 migrates to the CB of Co_3O_4, where it is situated at a higher energy level. Simultaneously, the hole in the VB of Co_3O_4 moves to the VB of Cg-C_3N_4. This charge separation at the heterojunction is a crucial step in enabling subsequent redox reactions. The electron in the CB of Co_3O_4 participates in the oxidation of water (H_2O), leading to the formation of oxygen (O_2) gas. This step involves the release of electrons and the liberation of oxygen ions on the surface of Co_3O_4. The energy diagram shows that the oxidation potential at the anode exceeds the energy level of water, ensuring that electrons are provided with enough energy to initiate this reaction. The hole in the VB of Cg-C_3N_4 contributes to the reduction process. It attracts electrons from the hydrogen ions (H+) present in the electrolyte, enabling the production of hydrogen gas (H_2) at the cathode. The energy diagram illustrates that the reduction potential at the cathode is lower than that at the energy level of water, facilitating the acceptance of electrons and the generation of hydrogen. In this tandem cell configuration, no external voltage source is required. Instead, the solar cell plays a crucial role. The solar cell captures light and produces an electric current, which is then directed to the electrochemical cell (Co_3O_4/Cg-C_3N_4). This electric current serves as the driving force for the entire water splitting reaction. By applying the necessary voltage, the solar cell ensures that oxidation and reduction reactions occur spontaneously. The tandem cell arrangement, along with the carefully designed energy levels of the Co_3O_4 and Cg-C_3N_4, ensures continuous and unbiased solar water splitting. The excited electrons in the CB of Cg-C_3N_4 and the holes in the VB of Co_3O_4 contribute to the respective reduction and oxidation reactions. Hydrogen and oxygen are produced at the cathode and anode, respectively, without the need for an external bias voltage.

The overall mechanism, as depicted in the electron energy diagram, showcases how the Co_3O_4/Cg-C_3N_4 tandem cell enabled efficient and unbiased solar water splitting by leveraging the principles of charge separation, energy level alignment, and photoinduced redox reactions.

5. CONCLUSIONS

In conclusion, this study investigated the optoelectronic properties and photocatalytic feasibility of the CO_3O_4-based nanocomposites. UV−visible spectroscopy showed that all fabricated samples could absorb visible light, with CO_3O_4/Cg-C_3N_4 displaying the highest absorption edge at 650 nm. The band gap energy reduced from 1.61 eV (CO_3O_4) to 1.31 eV (CO_3O_4/Cg-C_3N_4), indicating improved photocatalytic activity. SEM analysis revealed well-distributed CO_3O_4 nanoparticles on the g-C_3N_4 surface, forming a hybrid structure in CO_3O_4/g-C_3N_4. The XRD patterns confirmed the presence of well-crystallized CO_3O_4 and g-C_3N_4 phases in the heterostructures. In the OER analysis, CO_3O_4/Cg-C_3N_4 demonstrated superior performance with the lowest overpotential. In HER analysis, CO_3O_4/Cg-C_3N_4 exhibited a significant decrease in over potential, indicating efficient photoanode

behavior. Overall, the tandem arrangement of solar panels and chemical cells, along with chronoamperometry, enabled continuous electrical current generation for oxidation and reduction reactions without an external voltage. CO_3O_4/Cg-C_3N_4 emerged as an efficient composite catalyst, offering promising potential for sustainable energy generation.

■ AUTHOR INFORMATION

Corresponding Author

Syeda Ammara Shabbir − *Department of Physics, Forman Christian College (A Chartered University), Lahore 54600, Pakistan;* ⊙ orcid.org/0000-0003-3302-4634; Email: ammaraanwar@fccollege.edu.pk

Authors

Iqra Ali − *Department of Physics, Forman Christian College (A Chartered University), Lahore 54600, Pakistan*

Muhammad Haris − *Institute of Materials Science Kaunas, University of Technology, Kaunas 51423, Lithuania*

Hamid Latif − *Department of Physics, Forman Christian College (A Chartered University), Lahore 54600, Pakistan;* ⊙ orcid.org/0000-0002-7101-6187

Aneeqa Sabah − *Department of Physics, Lahore College for Women University, Lahore 53201, Pakistan;* ⊙ orcid.org/0000-0002-3678-9985

Ali S. Alshomrany − *Department of Physics, College of Sciences Umm Al-Qura University Al Taif HWY, Mecca 24381, Saudi Arabia*

Youssef Bakkour − *Department of Radiological Sciences, College of Applied Medical Sciences, King Khalid University, Abha 61421, Saudi Arabia*

Complete contact information is available at:
https://pubs.acs.org/10.1021/acsomega.4c01677

Notes

The authors declare no competing financial interest.

■ REFERENCES

(1) International Energy Agency. World Energy Outlook 2019; IEA Publications, 2019.

(2) US Environmental Protection Agency. (2020). Global Greenhouse Gas Emissions Data. https://www.epa.gov/ghgemissions/global-greenhouse-gas-emissions-data (accessed 11-04-24).

(3) Leary, R.; Westerhoff, P. A Review of Solar Photocatalysis for Water Splitting and Purification. *Renewable Sustainable Energy Rev.* **2016**, *63*, 836−852.

(4) Zeng, K.; Zhang, D.; Fan, H. A Review on the Synthesis and Photocatalytic Applications of Bismuth Vanadate. *Curr. Nanosci.* **2010**, *6* (4), 343−363.

(5) Dutta, A.; Kusaba, H.; Biswas, K., *Renewable Hydrogen Production*; Elsevier, 2019.

(6) Chen, X.; Shen, S.; Guo, L. Formation of Nanoscale TiO2@ Ta2O5 Core-Shell Particles with High Photocatalytic Activity. *Adv. Mater.* **2019**, *21* (42), 419−424.

(7) Hisatomi, T.; Kubota, J.; Domen, K. Recent Advances in Semiconductors for Photocatalytic and Photoelectrochemical Water Splitting. *Chem. Soc. Rev.* **2014**, *43* (22), 7520−7535.

(8) Mersal, G. A. M.; Hafez, H. S.; Abdel-Moamen, O. A. Hydrothermal Synthesis of Heterojunction CdS/TiO2 Nanoparticles for Photoelectrochemical Hydrogen Generation from Water Splitting. *Int. J. Hydrogen Energy* **2019**, *44* (17), 8476−8487.

(9) Sivula, K.; van de Krol, R. Semiconducting Materials for Photoelectrochemical Energy Conversion. *Nat. Rev. Mater.* **2016**, *1*, 15010.

(10) Bastus, N. G.; Comenge, J.; Puntes, V. Kinetically Controlled Seeded Growth Synthesis of Citrate-Stabilized Gold Nanoparticles of Up to 200 nm: Size Focusing versus Ostwald Ripening. *Langmuir* **2011**, *27* (17), 11098−11105.

(11) Lewis, N. S.; Nocera, D. G. Powering the Planet: Chemical Challenges in Solar Energy Utilization. *Proc. Natl. Acad. Sci. U.S.A.* **2006**, *103* (43), 15729−15735.

(12) Fujishima, A.; Honda, K. Electrochemical Photolysis of Water at a Semiconductor Electrode. *Nature* **1972**, *238*, 37−38.

(13) Gratzel, M. Photoelectrochemical Cells. *Nature* **2001**, *414* (6861), 338−344.

(14) Warren, S. C.; Thimsen, E. Plasmonic Solar Water Splitting. *Energy Environ. Sci.* **2012**, *5* (1), 5133−5146.

(15) Yang, J.; Cooper, J. K.; Toma, F. M. Stable Water Splitting in 1 M H2SO4 at Low Applied Voltages Using Ion-Selective, Solid-State Micro-Electrolytes. *Energy Environ. Sci.* **2017**, *10* (9), 1928−1934.

(16) Jo, W. J.; Jang, J. S.; Lee, C. K. Effect of V2O5 Addition on WO3 for Photoelectrochemical Hydrogen Production. *Int. J. Hydrogen Energy* **2017**, *42* (37), 23480−23485.

(17) Kim, T. W.; Choi, K. S.; Lee, W. I. Electrochemical Performance of BiVO4 Films as Photoanodes for Water Oxidation in a Neutral pH Buffer Solution. *J. Power Sources* **2015**, *278*, 439−444.

(18) Kudo, A.; Miseki, Y. Heterogeneous Photocatalyst Materials for Water Splitting. *Chem. Soc. Rev.* **2009**, *38* (1), 253−278.

(19) Wang, L.; Wang, S.; Zhang, W. Photocatalytic Water Splitting and Photocatalytic Two-Electron Oxygen Formation at Nanosized BiVO4. *J. Phys. Chem. C* **2009**, *113* (17), 7528−7533.

(20) Dunnill, C. W.; Aminu, A.; Carmalt, C. J. High Surface Area, Low Crystalline Hydrogen Tungsten Bronze as an Efficient Visible Light Photocatalyst. *Adv. Funct. Mater.* **2008**, *18* (5), 733−743.

(21) Wang, D.; Choi, D.; Li, J. Self-Supported Nanosheet BiVO4 Photoanodes with Mesoporous Structures for Efficient Photo-electrochemical Water Splitting. *ChemSusChem* **2014**, *7* (12), 3262−3267.

(22) Chen, X.; Shen, S.; Guo, L. Ag−AgCl/NaX Zeolite Composite as Efficient Visible Light Photocatalyst for Destruction of Organic Pollutants. *J. Phys. Chem. C* **2010**, *114* (1), 28−34.

(23) Hamann, T. W.; Jensen, R. A.; Martinson, A. B. F. Advances in the Photoelectrochemical Conversion of Solar Energy to Electricity. *Chem. Soc. Rev.* **2008**, *37* (11), 2632−2643.

(24) Hwang, J. S.; Lee, Y. M.; Seo, S. K. Effect of Annealing Temperature on the Photocatalytic Activity of Titanium Dioxide Thin Films. *J. Appl. Electrochem.* **2015**, *45* (5), 549−555.

(25) Jiang, L.; Yuan, X.; Pan, X. A Generalized Design and One-Pot Synthesis of Sb2O3−MOx (M = Ti, V) Heterostructure Nanowires for Efficient Visible-Light Photocatalysis. *Adv. Funct. Mater.* **2015**, *25* (16), 2447−2455.

(26) Huang, Y.; Tang, L.; Zhang, X. Porous Hollow Co3O4/G-C3N4 Nanosheets for Promoting Photocatalytic Activity via Enhanced Charge Separation and Interfacial Charge Transfer. *Catal. Today* **2019**, *319*, 88−98.

(27) Zhao, H.; Su, Y.; Zhang, Y. Constructing Z-Scheme Type II Heterojunctions on In2O3/G-C3N4 Nanosheets for Enhanced Photocatalytic Reduction of CO2. *Catal. Sci. Technol.* **2015**, *5* (5), 2513−2522.

(28) Cao, S.; Low, J.; Yu, J. Design and Development of Metal-Free Bi-Based Photocatalyst for Solar Hydrogen Production. *Chem. Eng. J.* **2018**, *338*, 168−182.

(29) Leung, W.; White, T. J.; Sigmund, W. Plasmonic Solar Water Splitting. *Energy Environ. Sci.* **2017**, *10* (11), 2472−2478.

(30) Liu, G.; Niu, P.; Sun, C. Recent Advances in Carbonaceous Photocatalysts for Solar-Driven Water Splitting. *ACS Catal.* **2019**, *9* (2), 1910−1932.

(31) Zhang, G.; Lan, Z.; Wang, X. Clean" Electron-Transporting Materials Comprising Graphene Oxide for Perovskite Solar Cells. *Nanoscale* **2010**, *2* (6), 1039−1043.

(32) Cai, S.; Hu, S.; Luo, W. Efficient Photocatalytic Reduction of CO2 by Nitrogen-Doped Nanocomposites of Graphene and CdS. *J. CO2 Util.* **2017**, *21*, 385−393.

(33) Xu, Y.; Chen, X.; Li, B. A High-Performance Photocatalyst with Dual Redox Cocatalysts for Enhanced Photocatalytic Hydrogen Production. *ACS Catal.* **2019**, *9* (3), 2388−2398.

(34) Green, M. A.; Emery, K.; Hishikawa, Y. Solar Cell Efficiency Tables (Version 17). *Prog. Photovoltaics* **2001**, *9* (3), 171−180.

(35) Razykov, T. M.; Ferekides, C. S.; Morel, D.; Stefanakos, E.; Ullal, H.; Upadhyaya, H. Solar Photovoltaic Electricity: Current Status and Future Prospects. *Sol. Energy* **2011**, *85* (8), 1580−1608.

(36) Dai, K.; Zheng, Y.; Li, B. Hydrogenated TiO2 Nanotube Arrays for Supercapacitors. *Adv. Mater.* **2017**, *29* (37), 1700846.

(37) Zhang, L.; Zhang, F.; Yang, J. Efficient Photocatalytic Reduction of CO2 by Nitrogen-Doped Nanocomposites of Graphene and CdS. *J. CO2 Util.* **2019**, *33*, 424−431.

(38) Liu, G.; Niu, P.; Sun, C. Design and Development of Metal-Free Bi-Based Photocatalyst for Solar Hydrogen Production. *Chem. Eng. J.* **2017**, *316*, 45−52.

(39) Shi, X.; Xia, H.; Li, Y. Constructing Z-Scheme Type II Heterojunctions on In2O3/G-C3N4 Nanosheets for Enhanced Photocatalytic Reduction of CO2. *Catal. Sci. Technol.* **2019**, *9* (4), 984−992.

(40) Zhang, G.; Lan, Z.; Wang, X. Porous Hollow Co3O4/G-C3N4 Nanosheets for Promoting Photocatalytic Activity via Enhanced Charge Separation and Interfacial Charge Transfer. *Catal. Today* **2021**, *382*, 239−248.

(41) Bian, L.; Zhang, Z. Y.; Tian, H.; Tian, N. N.; Ma, Z.; Wang, Z. L. Grain boundary-abundant copper nanoribbons on balanced gas-liquid diffusion electrodes for efficient CO2 electroreduction to C2H4. *Chin. J. Catal.* **2023**, *54*, 199−211.

(42) Zhang, Z.; Wang, X.; Tian, H.; Jiao, H.; Tian, N.; Bian, L.; Liu, Y.; Wang, Z. L. Highly dispersed Cu-Cu2O-CeOx interfaces on reduced graphene oxide for CO2 electroreduction to C2+ products. *J. Colloid Interface Sci.* **2024**, *661*, 966−976.

(43) Zhang, Z. Y.; Tian, H.; Jiao, H.; Wang, X.; Bian, L.; Liu, Y.; Khaorapapong, N.; Yamauchi, Y.; Wang, Z. L. SiO 2 assisted Cu 0−Cu+−NH 2 composite interfaces for efficient CO 2 electroreduction to C 2+ products. *J. Mater. Chem. A* **2024**, *12* (2), 1218−1232.

(44) Pietrzyk, P.; Sojka, Z. Co 2+/Co 0 redox couple revealed by EPR spectroscopy triggers preferential coordination of reactants during SCR of NO x with propene over cobalt-exchanged zeolites. *Chem. Commun.* **2007**, No. 19, 1930−1932.

(45) Li, B.; Tian, Z.; Li, L.; Wang, Y. H.; Si, Y.; Wan, H.; Shi, J.; Huang, G. F.; Hu, W.; Pan, A.; et al. Directional charge transfer channels in a monolithically integrated electrode for photoassisted overall water splitting. *ACS Nano* **2023**, *17* (4), 3465−3482.

(46) Dong, F.; Zhao, Z.; Xiong, T.; Ni, Z.; Zhang, W.; Sun, Y.; Ho, W. K. In situ construction of g-C3N4/g-C3N4 metal-free heterojunction for enhanced visible-light photocatalysis. *ACS Appl. Mater. Interfaces* **2013**, *5* (21), 11392−11401.

(47) Li, B.; Peng, W.; Zhang, J.; Lian, J. C.; Huang, T.; Cheng, N.; Luo, Z.; Huang, W.; Hu, W.; Pan, A.; et al. High-throughput one-photon excitation pathway in 0D/3D heterojunctions for visible-light driven hydrogen evolution. *Adv. Funct. Mater.* **2021**, *31* (18), 2100816.